A more defective substrate leads to a less defective passive layer: Enhancing the mechanical strength, corrosion resistance and anti-inflammatory response of the low-modulus Ti-45Nb alloy by grain refinement

Nan Hu[1], Lingxia Xie[1], Qing Liao[1], Ang Gao[1], Yanyan Zheng[1], Haobo Pan[1], Liping Tong[1*], Dazhi Yang[2*], Nong Gao[3], Marco J. Starink[3], Paul K. Chu[4], Huaiyu Wang[1*]

[1] Center for Human Tissues and Organs Degeneration, Shenzhen Institutes of Advanced Technology, Chinese Academy of Sciences, Shenzhen, China

[2] Department of Spinal Surgery, The 6th Affiliated Hospital of Shenzhen University Health Science Center, Shenzhen, China

[3] Engineering Materials group, University of Southampton, Southampton SO17 1BJ, UK

[4] Department of Physics, Department of Materials Science and Engineering, and Department of Biomedical Engineering, City University of Hong Kong, Tat Chee Avenue, Kowloon, Hong Kong, China

E-mail: lp.tong@siat.ac.cn (L.P. Tong); dazhiyang@email.szu.edu.cn (D.Z. Yang); hy.wang1@siat.ac.cn (H.Y. Wang)

Abstract

Orthopedic and dental implants made of β-type Ti alloys have low elastic modulus which can better relieve the stress shielding effects after surgical implantation. Nevertheless, clinical application of β-type Ti alloys is hampered by the insufficient mechanical strength and gradual release of pro-inflammatory metallic ions under physiological conditions. In this study, the β-type Ti-45Nb alloy is subjected to high-pressure torsion (HPT) processing to refine the grain size. After HPT processing, the tensile strength increases from 370 MPa to 658 MPa due to grain boundary strengthening and at the same time, the favorable elastic modulus is maintained at a low level of 61-72 GPa because the single β-phase is preserved during grain refinement. More grain boundaries decrease the work function and facilitate the formation of thicker and less defective passive films leading to better corrosion resistance. In addition, more rapid repair of the passive layer mitigates release of metallic ions from the alloy and consequently, the inflammatory response is suppressed. The results reveal a strategy to simultaneously improve the mechanical and biological properties of metallic implant materials for orthopedics and dentistry.

1. Introduction

Titanium (Ti) and its alloys are widely used metallic biomaterials for hard tissue replacement due to the high specific strength, good corrosion resistance, and adequate biocompatibility [1]. However, the elastic modulus of the conventional α-type pure Ti and α + β-type Ti-6Al-4V alloy is 104-114 GPa, which is larger than that of natural bones (10-30 GPa) [2, 3]. As a consequence, the implant will bear the majority of the mechanical load leading to the stress shielding effect after implantation, resulting in possible implant loosening and failure. Moreover, the alloying elements in the Ti-6Al-4V alloy raise clinical concerns about the biosafety and inflammatory reactions [4].

Recently, β-type Ti alloys with low elastic moduli have been fabricated with biologically friendly alloying elements such as niobium (Nb), molybdenum (Mo), tantalum (Ta), and zirconium (Zr) [5]. Among the different types of binary β-type titanium alloys with a body-centered cube (bcc) lattice, the Ti-45Nb alloy with a single β-phase [2, 3, 6] is especially attractive on account of the small elastic modulus of 60-70 GPa [7] and favorable osteogenic properties of Nb [8]. However, low-modulus Ti alloys usually have insufficient mechanical strength [2, 9]. Traditional heat treatment can improve the strength of β-type Ti alloys *via* precipitation hardening but unfortunately, the elastic modulus increases at the same time [10, 11] due to unavoidable changes in the crystalline structure. Moreover, the hardening precipitates may reduce the corrosion resistance of β-type Ti alloys [12, 13]. Alternatively, grain boundary hardening at room temperature provides the possibility to increase the strength based on the Hall-Petch relationship [14] without changing the elastic modulus [6]. Severe plastic deformation (SPD) is commonly adopted to fabricate ultra-fine-

grained (UFG) materials by introducing extremely high plastic strain to the metals [15].

In fact, SPD techniques such as rolling and folding (R&F) [6], high-pressure torsion

(HPT) [1,3,9], and hydrostatic extrusion (HE) [16] have been shown to enhance the

strength of Ti-45Nb alloys by producing a ultra-fine-grained (UFG) structure with

unchanged elastic moduli. However, orthopedic and dental biomaterials must fulfill

multiple requirements besides the mechanical properties. Under *in vivo* conditions, the

metallic implants are frequently in contact with an aggressive medium and significant

leaching of metallic ions from the implants is possible [17]. Therefore, sufficient

corrosion resistance and biocompatibility are also critical to metallic implants.

The effects of grain refinement on the corrosion resistance and biological response

of Ti-45Nb alloys are not well understood as there are multiple factors in addition to

conflicting results [18]. Therefore, it is necessary to investigate systematically the

influence of grain boundaries on the surface passivity. A native passive oxide film

forms on Ti and its alloys upon exposure to air [12] and the properties of the passive

oxide layer are mainly determined by the stoichiometry and defects [19], both of which

are affected by the grain size of the materials. The passive layer on the Ti-45Nb alloy

is mainly composed of TiO_2, Nb_2O_5, and their sub-oxides [14] and TiO_2 is more

corrosion resistant when doped with Nb_2O_5 [14, 20, 21]. Hence, the influence of grain

size on the chemical composition of the passive layer (TiO_2, Ti_2O_3, TiO, Nb_2O_5, NbO_2,

and NbO) should be assessed quantitatively. Moreover, defects also change the

properties of the passive layer [22]. Nanoscale grain refinement has been reported to

improve the anti-corrosion behavior of α-type pure Ti [23] as well as β-type alloys such

as Ti-29Nb-13Ta-4.6Zr [24] and Ti–24Nb–4Zr–8Sn [25] by reducing the number of

defects and increasing the thickness of the passive layer. In addition, the properties of

the passive films are crucial to the biological response *in vivo* [4,14]. If the passive

layer is damaged, exfoliated, or dissolved, the corrosion products and released ions may cause detrimental side effects and eventual implant failure [26, 27]. In general, metallic ions released from implants can activate the immune system [28] to cause inflammation and produce cytotoxicity to the peri-implant macrophages. Therefore, the desirable metallic implants should be optimized by tailoring the surface passive film [4, 29] in conjunction with mitigation of metallic ions release.

In this study, the effects of grain refinement on the Ti-45Nb alloy are studied in details in order to elucidate the relationship between the grain size, microstructure, and properties of the surface passive layer. The biomedical Ti-45Nb alloy is subjected to HPT processing and the influence of grain refinement on the corrosion resistance are investigated systematically by a variety of electrochemical measurements as well as in-depth examination on the microstructure of the passive layer. As a potential biomaterial for orthopedics and dentistry, the inflammatory response of the UFG Ti-45Nb alloy is evaluated both *in vitro* and *in vivo*.

2. Material and methods

2.1 HPT processing

The elemental composition of Ti-45Nb bars obtained from Ningxia Orient Tantalum Industry Co. Ltd. was determined by inductively-coupled plasma optical emission spectrometry (ICP-OES) on a Perkin Elmer OPTIMA 7000DV spectrometer (Table S1, Supporting Information). Ti-45Nb disks with a thickness of 0.8 mm and diameter of 10 mm were cut and then processed by HPT at room temperature under an applied pressure of 3.0 GPa at a rotational speed of 1 revolution per minute (rpm) for 0.25-10 revolutions and under quasi-constrained conditions. The coarse-grained

sample before HPT processing was designated as CG and after HPT processing for 0.25, 1, 4 and 10 turns, the samples were designated as 0.25T, 1T, 4T and 10T, respectively.

2.2 Microstructure of Ti-45Nb

The samples were ground with SiC abrasive paper of 800, 1200, 2500 and 5000 grit and polished with 3, 1, and 0.05 μm diamond suspensions successively. Etching was conducted in an acidic solution containing 2 vol% HF, 5 vol% HNO_3, and 93 vol% H_2O. Optical microscopy (OM, Leica DM4M) was carried out and the linear intercept method was implemented to measure the grain size of the CG sample. Transmission electron microscopy (TEM, JEM 3010) was conducted at 300 kV to examine the grain size of the UFG samples. The TEM samples were prepared by twin-jet electropolishing at 30 V in a solution containing 6 vol% $HClO_4$ + 34 vol% 1-butanol + 60 vol% methanol at -30 to -25 °C. Selected-area electron diffraction (SAED) was performed on the TEM sample with a spot size of 720 nm. The grain diameter was estimated by measuring and averaging the length and width of 60 of the strongly diffracting grains using ImageJ® software [30] from 4 different TEM samples. X-ray diffraction (XRD) was carried out on a D8 ADVANCE diffractometer with monochromatic Cu $K_α$ radiation, step size of 0.02°, and step time of 0.25 s between 20° and 90° (2θ).

2.3 Mechanical properties of Ti-45Nb

A Matsuzawa Seiki MHT-1 microhardness tester was employed to determine the Vickers microhardness using a weight of 1000 g and dwell time of 15 s. Prior to the microhardness test, the samples were ground with SiC abrasive paper with 800, 1200, 3000 and to 5000 grit successively. The tensile tests were performed in triplicate on a CMT6103 universal testing machine with a load resolution of 0.1 N. The miniature tensile specimens (Figure S1, Supporting Information) with a 4 mm gauge length and 1 mm width were machined from the HPT disks by electro-discharge machining. The

ultimate tensile strength (UTS) was determined from the tensile curve and the percent of elongation was calculated based on the elongated length of the gauge after fracture. Nanoindentation measurements were performed on a Keysight Nano Indenter G200 equipped with a Berkovich indenter tip and calibrated by the nanoindentation measurements using a fused silica reference sample over a wide load range. Ten nanoindentations with a maximin load of 650 mN were performed on each sample at a rate of 10 nm/s and the test locations were at least 50 μm apart. The method of Oliver and Pharr was employed to determine the elastic modulus from the load-displacement curves with the Poisson's ratio assumed to be 0.41 [31].

2.4 Electrochemical measurements

The electrochemical assessment was conducted on a CHI660D electrochemical workstation (CH Instruments, Inc.). A circular area with a diameter of 6 mm was exposed to the electrolyte and the rest of the sample was sealed with a copper cable by corrosion-resistant butyl tapes. Before corrosion tests, all the samples were ground with 5000-grit abrasive papers and then recorded for the surface profiles using infinite focus optical microscopy on an Alicona non-contact profilometer. A total of five measurements were made per sample to allow calculation of mean and standard deviation. The ASME B46.1-2002 standard was used to calculate the average surface roughness (Ra) of different samples. A conventional three-electrode configuration was adopted in the electrochemical studies conducted in 70 ml of deaerated Hank's solution (GIBCO®) (Composition specified in Table S2, Supporting Information) as the simulated body fluid (SBF) at 37 ± 0.5 °C maintained by a heating jacket. The Ti-45Nb sample was the working electrode, whereas the 1 cm^2 platinum plate and saturated calomel electrode (SCE) were the counter and reference electrodes, respectively. Each sample was immersed in SBF for 1 h to esta blish the open circuit potential (E_{ocp}) and

then an alternating sinusoidal potential of 10 mV was applied. Electrochemical impedance spectroscopy (EIS) was carried out in the frequency range between 10 mHz and 100 kHz and potentiodynamic polarization was then conducted in the potential range between -1.5 and 0.5 V at a scanning rate of 1 mV. The potential (E)-current density (j) data were plotted as Tafel plots of E vs. log (j) and the corrosion current density (J_{corr}) was derived from the Tafel plots [32] to study the influence of grain refinement on the electrochemical resistance of Ti-45Nb alloys [18]. Mott-Schottky (MS) experiments were performed in the potential range of -1.5 to 0.5 V (vs. SCE) with an applied frequency of 1 kHz. In the electrochemical experiments, the SBF solution was changed for each sample and all the electrochemical tests were repeated three times to improve the statistics.

2.5 Leaching of metallic ions

The samples were ground with SiC abrasive paper with 800, 1200, 3000, and 5000 grit successively and cleaned ultrasonically. Five double-sided ground samples with a total surface area of 7.85 cm^2 were immersed in 15 mL of SBF at 37 ± 1 ˚C for up to 7 days. The concentrations of Ti and Nb released to the solution were determined by inductively-coupled plasma mass spectrometry (ICP-MS) on a Thermo Scientific iCAPQ spectrometer. The quantity of metal ion release was calculated using the following formula: (15 mL) × [(metal concentration) -(blank)]/ (total surface area). A test solution without the metal specimens was used as the blank. The calibration curves were obtained from five points with increasing concentrations in the standard solution. Prior to performing ICP-MS, acid digestion was carried out to digest the organic components using nitric acid.

2.6 Surface characterization

X-ray photoelectron spectroscopy (XPS) was performed on the ESCALAB 250Xi

(Thermo Fisher) with monochromatic Al K$_\alpha$ X-ray. The binding energies of Ti 2p and Nb 3d were determined at a pass energy of 50 eV with a resolution of 0.1 eV referenced to C 1s (284.8 eV). The in-depth composition of the surface passive layer was determined by XPS with argon sputtering for 0-150 s. Ultraviolet photoelectron spectroscopy (UPS) was performed on the same machine with an ultraviolet source energy He I ($hv = 21.22$ eV) at a pressure of approximately 5.5×10^{-8} mbar and 2 eV pass energy. Before the measurement, argon sputtering was performed for 3 min to remove surface contaminants. A negative bias of 10 V was applied to the sample to shift the spectra from the spectrometer threshold and the energy resolution was 0.1 eV.

2.7 Viability of HMSCs

The human mesenchymal stem cells (HMSCs) were obtained from the American Type Culture Collection (ATCC) and maintained in the culture medium composed of the 89% α-MEM basic medium (Hyclone), 10% fetal bovine serum (Corning), and 1% penicillin-streptomycin (Invitrogen). Sterilization was performed with ultraviolet light on both sides of the sample for 30 min before cell seeding. In the biological assays, the HMSCs were seeded with a density of 2×10^4 cells per sample on 24-well tissue culture plates and the cell counting kit-8 (CCK-8) was used to determine the viability of cultured HMSCs. After incubation for 1, 3 and 7 days (denoted as 1D, 3D and 7D), the cell culture medium was collected and the samples were washed three times with the sterile phosphate buffer saline (PBS) solution before 400 μL of the culture medium containing 10% CCK-8 were added. After incubation for another 2 h at 37 ˚C, 200 μL of the medium were transferred to another 96-well plate to measure the absorbance at a wavelength of 450 nm on a microplate reader (BL340, Biotech, USA).

2.8 Biological response of RAW264.7 cells

The RAW264.7 cells obtained from ATCC were maintained in in the culture medium composed of the high-glucose dulbecco's minimum essential medium (Hyclone), 10% fetal bovine serum (Corning), and 1% penicillin-streptomycin (Invitrogen). The RAW264.7 cells were seeded on the samples with a density of 2×10^4 cells per sample. After incubation for 1 and 3 days, CCK-8 was utilized to determine the viability of RAW264.7 cells as described above. The samples with cells were rinsed with sterile PBS three times, fixed with 2.5% glutaraldehyde, dehydrated with 30%, 40%, 50%, 70%, 90% and 100% (v/v) ethanol for 15 min each, dried in air, sputter-coated with platinum, and examined for the cell morphology by SEM. At the same time points, the cell culture supernatant was collected and centrifuged at 2,000 rpm for 5 min. The secreted TGF-β1 and TNF-α were detected by the TGF-β1 Valukine ELISA Kit (R&D system) and TNF-α Valukine ELISA Kit (R&D system) according to the manufacturer's instruction.

2.9 *In vivo* study

The animal procedures and experiments were approved by the Ethics Committee for Animal Research, Shenzhen Institutes of Advanced Technology, Chinese Academy of Sciences. The male and 8 weeks old Sprague Dawley (SD) rats were used and the CG and 10T samples were subcutaneously implanted into the symmetrical sides of the dorsal midline of SD rats to evaluate the *in vivo* anti-inflammation effects. Before surgery, each rat was anesthetized with 2% pentobarbital sodium (2.3 mL·kg^{-1}) *via* intraperitoneal injection. The dorsal area of each rat was shaved followed by sterilization using povidone iodine. A longitudinal surgical incision was made and implanted with the samples and the incision was sutured. After implantation for 1, 3 and 7 days, the rats were euthanized and the subcutaneous tissues were harvested, fixed

in 4% paraformaldehyde, embedded with paraffin, and sectioned for hematoxylin and eosin (H&E) staining and immunohistochemistry evaluation. The immunohistochemistry evaluation was performed with antibodies of INOS (M1 marker) and CD163 (M2 marker) as well as the corresponding secondary antibodies (Servicebio, China). 4',6-diamidino-2-phenylindole (DAPI, Servicebio, China) was used for nucleus counterstaining and the specimens after staining were examined by fluorescent microscopy (Nikon Eclipse CI, Japan).

2.10 Statistical analysis

All the values were expressed as mean ± standard deviation. The *in vitro* and *in vivo* assays were performed in triplicate and each *in vitro* experiment was repeated three times with the data from a representative experiment shown. Independent t-tests were performed to determine the statistical significance. A difference at $p < 0.05$ was considered to be significant and that at $p < 0.01$ or $p < 0.001$ was considered to be highly significant.

3. Results

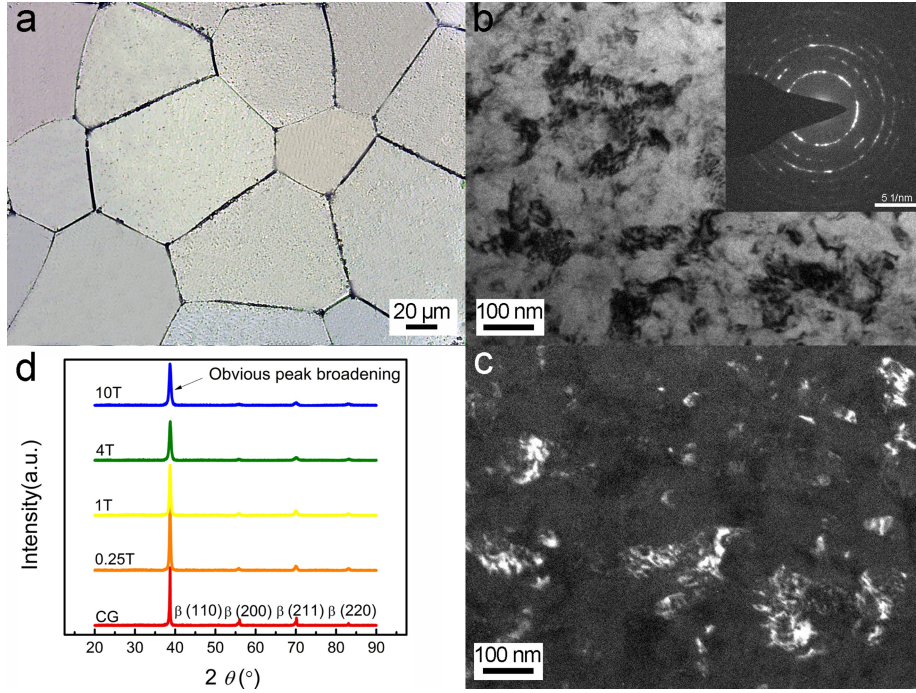## 3.1 Grain size and mechanical properties

Figure 1. Sample characterization: (a) OM images of the CG sample; (b) Bright-field TEM image (SAED as an inset) and (c) Dark-field TEM image of the 10T sample; (d) XRD patterns of the samples after HPT processing for 0, 0.25, 1, 4 and 10 turns.

As shown by the OM image in Figure 1a, the CG sample shows a mean grain size of 77 ± 12 μm. After 10-turn HPT processing, the curvy and not well-defined grain boundaries in the TEM images (Figure 1b-c) indicate the typical non-equilibrium feature of grain boundaries generated by SPD processing [33]. Those grains with poorly defined boundaries are different from grain boundaries in most conventionally processed materials [34]. The grain size of the Ti-45Nb alloy is refined homogeneously to 88 ± 35 nm (Figure 1b and c) and the distribution of grain sizes is shown in Figure S2 (Supporting Information). It should be noted that grain sizes measured from dark field images can slightly underestimate the grain size due to distorted layers at the periphery of each grain [35].

12

The SAED pattern of the 10T sample shows spots arranged in circles (Figure 1b inset), indicating the presence of several grains with high angle grain boundaries in a small area [35] and a UFG microstructure. The XRD patterns in Figure 1d show that the Ti-45Nb samples have the bcc crystalline structure as only peaks from the β phase, that are (110), (200), (211), and (220) planes, can be identified after HPT processing for 0, 0.25, 1, 4 and 10 turns. Evidently, HPT processing does not induce phase transformation but instead leads to severe strain and significant grain refinement resulting in significant peak broadening [3].
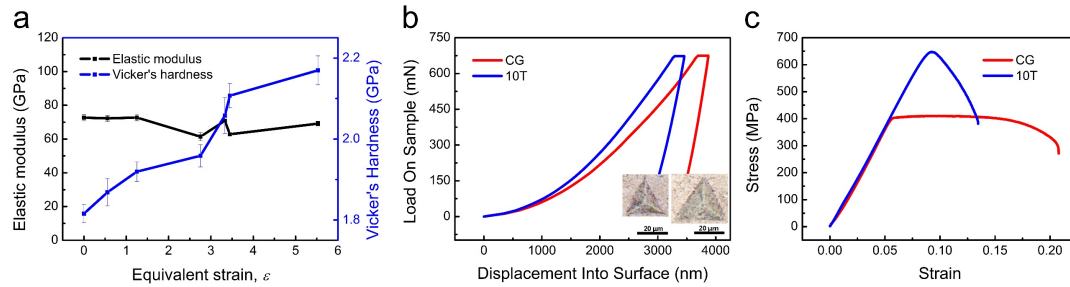

Figure 2. Mechanical properties of the Ti-45Nb alloy before and after HPT processing: (a) Elastic modulus and microhardness; (b) Nanoindentation curves and areas; (c) Tensile curves.

Figure 2 shows the mechanical properties of the Ti-45Nb alloy before and after HPT processing. Figure 2a discloses that HPT processing increases the microhardness of the Ti-45Nb alloy as the equivalent strain ε increases. Specifically, the microhardness increases from 1.81 GPa for the CG sample ($\varepsilon = 0$) to 2.17 GPa for the 10T sample ($\varepsilon = 5.5$ at the edge area) and more details are shown in Figure S3 (Supporting Information). In contrast, the elastic modulus of the HPT-processed Ti-45Nb alloy (61-72 GPa) shows some ups and downs with increasing ε, which are close to the reported values [3,16,36]. The variations of detected elastic modulus can be

attributed to the rolling texture after HPT processing [16,36].

Figure 2b displays the load versus displacement curves during nanoindentation and corresponding indentation areas. The 10T sample exhibits a smaller displacement as well as smaller indentation area than the CG sample confirming the larger microhardness after HPT processing. The tensile curves in Figure 2c show that the CG and 10T samples have similar elastic moduli according to almost the same slopes of the linear parts (strain 0.00-0.05). On the other hand, the ultimate tensile strength of the Ti-45Nb alloy increases from 370.6 ± 35.7 MPa to 658.4 ± 12.2 MPa after HPT processing for 10 turns. Although HPT processing reduces the ductility of alloys [37], as the elongation decreases from $16.6\% \pm 1.7\%$ of the CG sample to $8.3\% \pm 1.5\%$ of the 10T sample, the final ductility is sufficient for clinical application according to the specification of ASTM F67-13 [38]. Overall, HPT processing improves the strength of the Ti-45Nb alloy with good ductility but does not increase the elastic modulus.
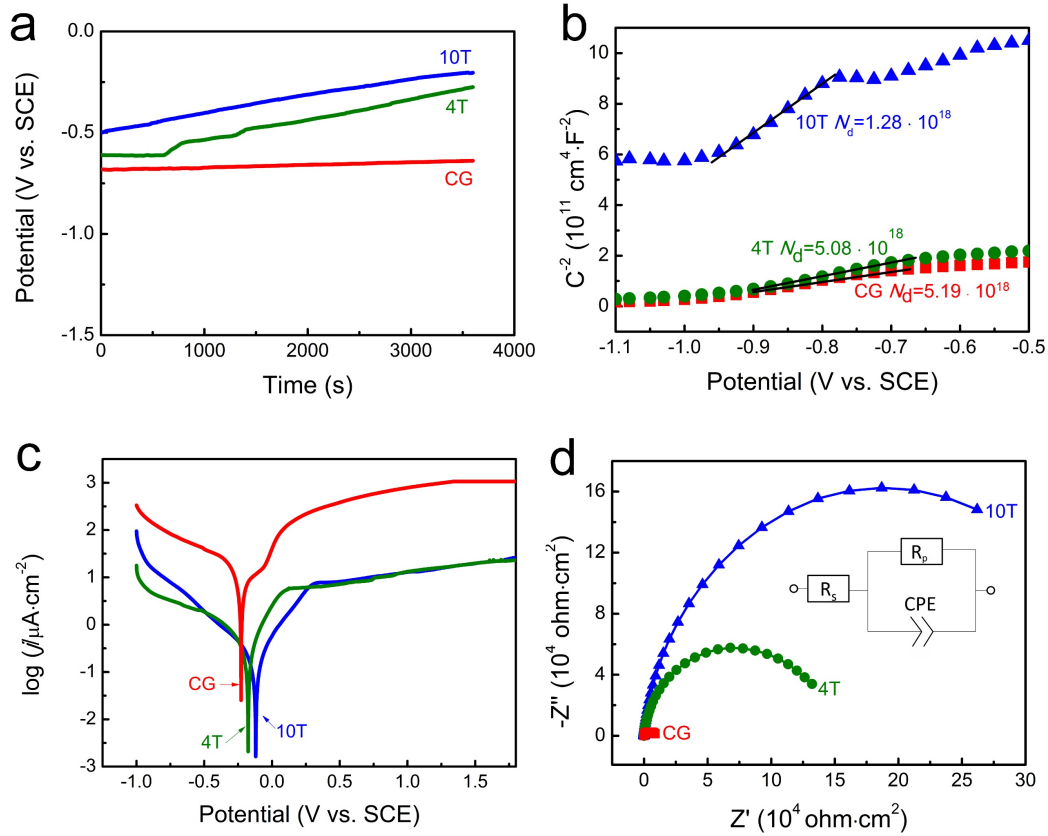
3.2 Electrochemical properties

Figure 3. Electrochemical properties of the Ti-45Nb samples: (a) OCP-time curves; (b) MS plots with N_d (unit: cm^{-3}) marked for each sample; (c) Tafel plots; (d) Nyquist plots.

By immersing the GG, 4T and 10T samples in SBF at 37 ˚C, the corrosion resistance is evaluated by open circuit potential (OCP)-time measurements, MS plots, anodic polarization and EIS measurements. OCP is the potential of the working electrode relative to the reference electrode without an applied current to reflect the thermodynamic equilibrium at the metal/electrolyte interface as a function of time. As shown in Figure 3a, the OCP curves become electro-positive with immersion time indicating constant inhibition of the anodic reaction (passivation) [39]. After SBF immersion for 1 h, the OCPs of the CG, 4T, and 10T samples are -0.639, -0.275, and -0.204 V, respectively, suggesting that corrosion resistance follows the order of 10T >

15

4T > CG. The passive film formed on Ti-based materials is an n-type semiconductor [25] and MS plots are utilized to characterize the change in the donor density (N_d) of the passive film. As shown in Figure 3b, the applied potential E and C^{-2} (C is the capacitance of the space charge layer) show a clear linear relationship and positive slopes in the marked range. The results corroborate that the passive layers are n-type semiconductors [40]. Point defects such as oxygen vacancies and/or Ti/Nb interstitials act as electron donors [40] and N_d is calculated from the MS plots according to the following relationship [36, 37]:

$$\left(\frac{1}{C^2}\right) = \frac{2}{\varepsilon\varepsilon_0 q N_d}\left(E - E_{fb} - \frac{kT}{q}\right),$$

where E_{fb} is flatband potential, ε is the dielectric constant ($\varepsilon = 55$ [43] for anatase) of oxide, ε_0 is the permittivity of vacuum (8.85×10^{-14} F/cm), and q, k, and T are the electronic charge (1.6×10^{-19} C), Boltzmann's constant (1.380649×10^{-23} J/K), and absolute temperature, respectively. N_d can be estimated from the slope of the MS plot by the following simplified equation [42]:

$$N_d = \frac{2}{\varepsilon\varepsilon_0 q}\left[\frac{d\left(\frac{1}{C^2}\right)}{dE}\right]^{-1}.$$

From the slopes of the linearly fitted plots in Figure 3b, the N_d values of the CG, 4T and 10T samples are 5.19×10^{18} cm^{-3}, 5.08×10^{18} cm^{-3}, and 1.28×10^{18} cm^{-3}, indicating less point defects (better protection) in the passive film after grain refinement. The potentiodynamic polarization results are presented as Tafel curves in Figure 3c and the corrosion potentials (E_{corr}) and corrosion current densities (J_{corr}) derived from the Tafel plots are given in Table 1. J_{corr} decreases but E_{corr} is electropositive after HPT processing indicating smaller corrosion rates. Furthermore, the well-defined passivation plateaus verify the passive corrosion mode of the Ti-45Nb samples.

Table 1. Electrochemical parameters of the Ti-45Nb alloys with different grain sizes.

Samples	OCP (V vs. SCE)	J_{corr} ($\mu A \cdot cm^{-2}$)	E_{corr} (V vs. SCE)	N_d ($10^{18}\,cm^{-3}$)
CG	-0.639 ± 0.045	8.55 ± 4.88	-0.228 ± 0.064	5.19 ± 0.57
4T	-0.275 ± 0.067	0.292 ± 0.105	-0.176 ± 0.031	5.08 ± 0.65
10T	-0.204 ± 0.034	0.213 ± 0.075	-0.120 ± 0.022	1.28 ± 0.23

Figure 3d shows the Nyquist plots of the Ti-45Nb samples and the equivalent electric circuit is presented in the inset with a single time constant to fit the EIS data [19]. It comprises three components: R_s - solution resistance, R_p - polarization resistance, and CPE - constant phase element for the interfacial capacitance. The reason for introducing CPE rather than a simple capacitor arises from the surface roughness and/or presence of defects in the crystal lattice (grain boundaries or dislocations) [9]. R_s depends on the distance between the sample and reference electrode and the shape of the corrosion cell is the same for all the samples (15 ± 1 $\Omega \cdot cm^2$). Generally, R_p is proportional to the diameter of the semi-circular Nyquist plots. The higher the value of R_p, the better are the anti-corrosion properties of the passive layer and consequently, the slower the corrosion process [19]. Therefore, the EIS results in Figure 3d indicate that the 10T sample has the best corrosion resistance. The surface morphology before and after the polarization test (Figure S4, Supporting Information) corroborates the tendency of the OCP, MS, Tafel and EIS results. Before corrosion tests, Ra of the CG and 10T samples is calculated to be 36.4 ± 4.8 nm and 31.7 ± 3.7 nm, respectively. There is no significant difference of surface roughness between the CG and 10T groups ($p > 0.05$). After polarization, the sample surfaces turn yellow due to oxidation and the CG sample is less corrosion resistant than the 10T sample as indicated by more
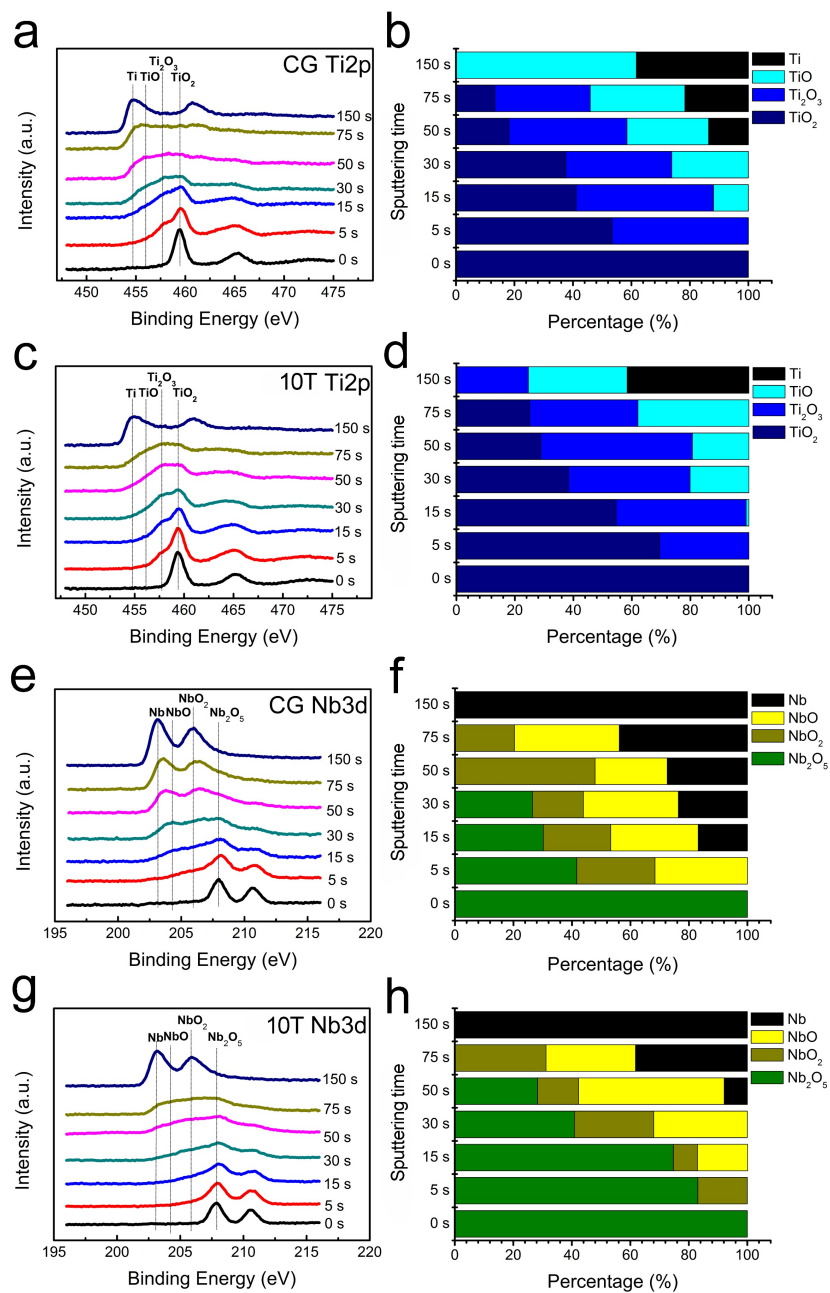
corroded areas with black dots.

3.3 Surface chemistry

Figure 4. Surface chemical states of the CG and 10T samples: (a, b) $TiO_2/Ti_2O_3/TiO/Ti$ peaks and percentages of the CG sample; (c,d) $TiO_2/Ti_2O_3/TiO/Ti$ peaks and percentages of the 10T sample; (e,f) $Nb_2O_5/NbO_2/NbO/Ti$ peaks and percentages of the CG sample; (g,h) $Nb_2O_5/NbO_2/NbO/Ti$ peaks and percentages of the 10T sample.

Since the corrosion resistance of the Ti-45Nb alloy is significantly improved after HPT processing, the chemical composition of the surface passive layers of the CG and 10T samples are determined by XPS as shown in Figure 4. There are four valence states of Ti (Ti-Ti^0, Ti^2, Ti^3 and Ti^4) and Nb (Nb-Nb^0, Nb^2, Nb^4 and Nb^5) in the high-resolution Ti 2p and Nb 3d spectra of the surface passive layer at different depths. For both the CG and 10T samples, the strong doublet ($Ti2p_{3/2}$ binding energy ~458.1-458.8 eV) is attributed to TiO_2 and the strong doublet ($Nb3d_{5/3}$, ~207.5-208.1 eV) stems from Nb_2O_5, indicating that the passive layer is mainly composed of TiO_2 and Nb_2O_5. After Ar^+ sputtering for 0, 5, 15, 30, 50, 75 and 150 s, the top layer of TiO_2 and Nb_2O_5 is removed and the underlying Ti_2O_3/TiO and NbO_2/NbO components are exposed until metallic Ti and Nb are reached. In the Ti 2p spectra, metallic Ti is revealed on the CG sample after Ar^+ sputtering for 50 s, but sputtering for 75 s of the 10T sample does not yet show metallic Ti (Figures 4a-d), indicating a thicker TiO_x (x = 1-2) layer on the latter sample. The Nb 3d spectra exhibit a similar tendency (Figure 4e-h) that the NbO_y (y = 1-2.5) layer on the 10T sample is thicker than that on the CG sample. According to the sputtering rate of Ta_2O_5 standard (0.2 nm/s) under the same condition, the estimated thickness of the passive layer on the CG and 10T samples are 6 and 15 nm, respectively. Metallic Nb is observed after sputtering for 15 s and 50 s of the CG and 10T samples, respectively, and it appears earlier than the metallic Ti counterpart (50 and 100 s). Therefore, the surface layer on NbO_y is thinner than that on TiO_x. The difference can be explained by the Ellingham–Richardson diagram [44]. Specifically, the standard free energy change (ΔG^Θ) of oxide formation is negatively correlated with the stability of the compound. In the large temperature range, $-\Delta G^\Theta$ of Ti is higher than that of Nb [44] and therefore, Nb is less able to form oxide under the conditions of low oxygen content leading to a thinner oxide layer.
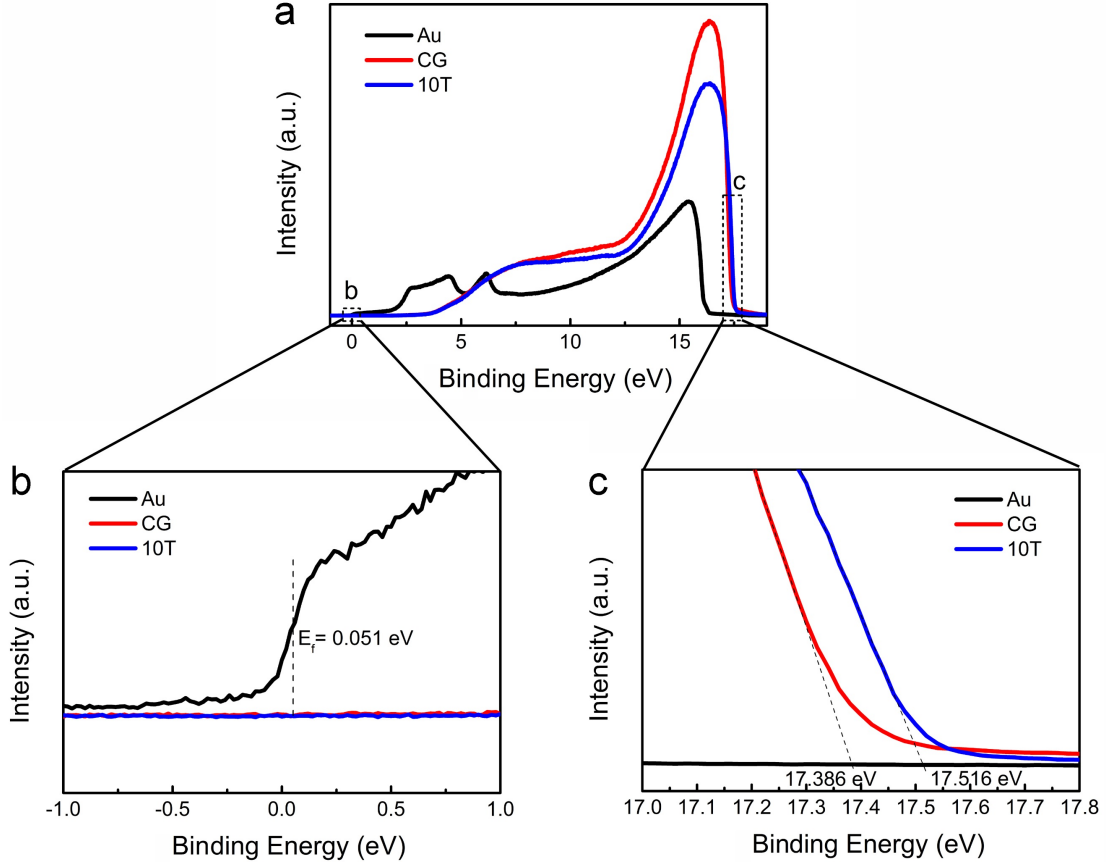
3.4 Surface work functions

Figure 5. Surface work functions of the CG and 10T samples: (a) UPS determined at a negative bias (-10 eV); (b) Magnified image of the area marked by b in (a) showing the Fermi edge of the standard Au sample for characterization; (c) Magnified image of the area marked by c in (a) showing the cut-off edges of the CG and 10T samples.

The surface work functions of the Ti-45Nb alloys with different grain sizes are determined by UPS as shown in Figure 5a. By measuring the width of the emitted electrons (W) from the secondary electron cutoff (E_{cutoff}) to the Fermi edge (E_f) as $W = E_{cutoff} - E_f$, and subtracting W from the energy of the incident UV light (hv), the work function Φ is given by the following equation [45]:

$$\Phi = hv - (E_{\text{cutoff}} - E_{\text{f}}),$$

where hv is the energy of the He I emission line (21.22 eV). To distinguish the secondary electron cutoff from low energy electron scattering, a negative bias voltage of 10 eV is employed in the work function assessment. The horizontal axes of the spectra in Figure 5a-b are corrected by 10 eV towards a positive direction and E_{f} of the Au standard sample is calculated to be 0.051 eV. Combined with the E_{cutoff} values shown in Figure 5c, the work functions Φ of the CG and 10T samples are calculated to be 3.885 eV and 3.755 eV, respectively. The results demonstrate that the surface electrons on the 10T sample are less bound than those on the CG sample and so less energy is required for electrons to escape from the surface of the 10T sample.

3.5 Ion release and biological performance *in vitro*

The immune response is a key factor that determines the *in vivo* fate of orthopedic biomaterials [46]. Herein, macrophages are cultured on the Ti-45Nb samples with different grain sizes to evaluate the cell viability and protein levels. Prior to the biological assays, the CG and 10T samples are immersed in SBF at 37 ˚C for up to 7 days and then release of Ti and Nb ions is evaluated. As shown in Figure 6a, the amounts of Ti and Nb ions released from the Ti-45Nb alloy are significantly reduced after HPT processing for 10 turns. In fact, release of metallic ions from dental implants has been observed to affect the biocompatibility, but the cytotoxicity decreases with less ion release.
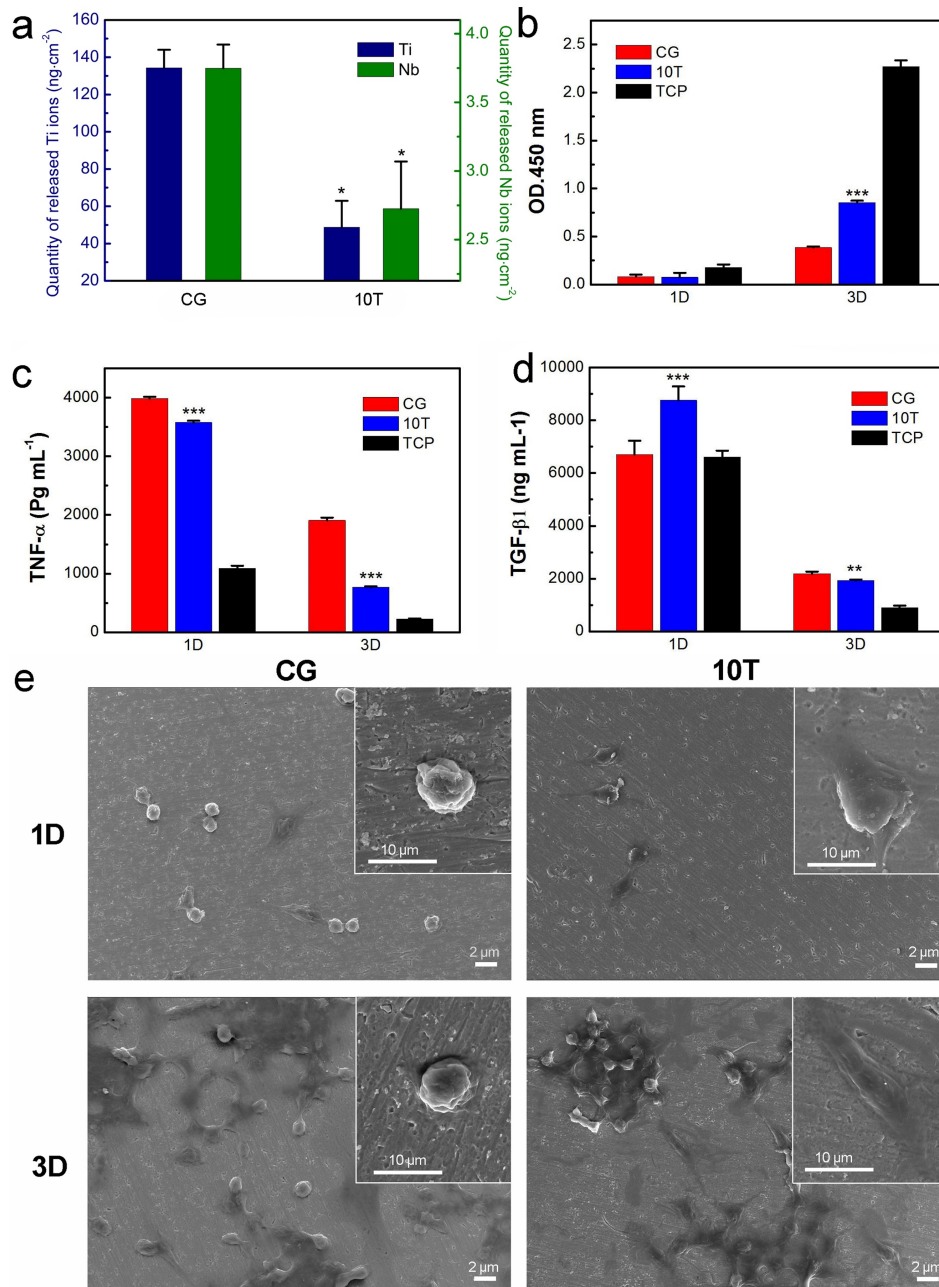
Figure 6. Ion release and biological performance *in vitro*: (a) Release of Ti and Nb ions after immersion in SBF at 37 ˚C for up to 7 days; (b) Time-dependent viability of macrophages cultured on the CG and 10T samples; (c) TNF-α and (d) TGF-β1 protein expressions of macrophages cultured on the CG and 10T samples; (e) SEM images of macrophages cultured on the CG and 10T samples for 1 and 3 days. * denotes $p < 0.05$, ** denotes $p < 0.01$ and *** denotes $p < 0.001$ compared with the CG group.

Figure 6b shows the viability of macrophages cultured on the CG and 10T samples and clearly, the 10T sample is better than the CG sample in supporting cell growth on account of reduced ion release. The samples are also seeded with HMSCs to evaluate the time-dependent viability (Figure S5, Supporting Information) and the better biocompatibility of the 10T sample is corroborated. The macrophages on the samples are determined quantitatively for protein release of pro-inflammatory TNF-α (Figure 6c) and anti-inflammatory TGF-β1 (Figure 6d). The 10T sample shows a smaller expression of pro-inflammatory cytokines (TNF-α) and larger expression of anti-inflammatory cytokines (TGF-β1) compared with the CG sample. With regard to the morphology of cells on the different samples (Figure 6e), macrophages on the CG sample exhibit an oval shape (M1-type), whereas those on the 10T sample are elongated in shape with abundant pseudopodia (M2-type) [47]. All in all, HPT processing alleviates the inflammatory response on the Ti-45Nb alloy *in vitro* by reducing release of undesirable metallic ions.

3.6 Inflammatory response *in vivo*

In order to examine the inflammatory response *in vivo,* the CG and 10T samples are implanted subcutaneously into the back of SD rats for 1, 3 and 7 days. As shown in Figure 7a, both the CG and 10T samples induce foreign body reactions (FBRs) *in vivo* by impacting macrophages at the peri-implant sites. Specifically, acute inflammation is triggered at 1 day post-implantation but the 10T sample shows less M1-type macrophages (red fluorescence) than the CG sample. At time points of 3 and 7 days post-implantation, acute inflammation fades and the M2-type macrophages with green fluorescence are more dominant on the 10T sample. Therefore, the 10T sample provides better anti-inflammatory effects. From the macroscopic view, all the rats show few abnormalities after implantation (Figure S6, Supporting Information), except that

the peri-implant tissues in the CG group are swollen on the 7th day (Figure 7b) as a typical symptom of inflammation.   The inflammatory states of the peri-implant tissues are further determined by H&E staining as shown in Figure 7c and d.   Evidently, the fibrous layers induced by the 10T sample are much thinner after 3 and 7 days of implantation corroborating less inflammation for the 10T group.
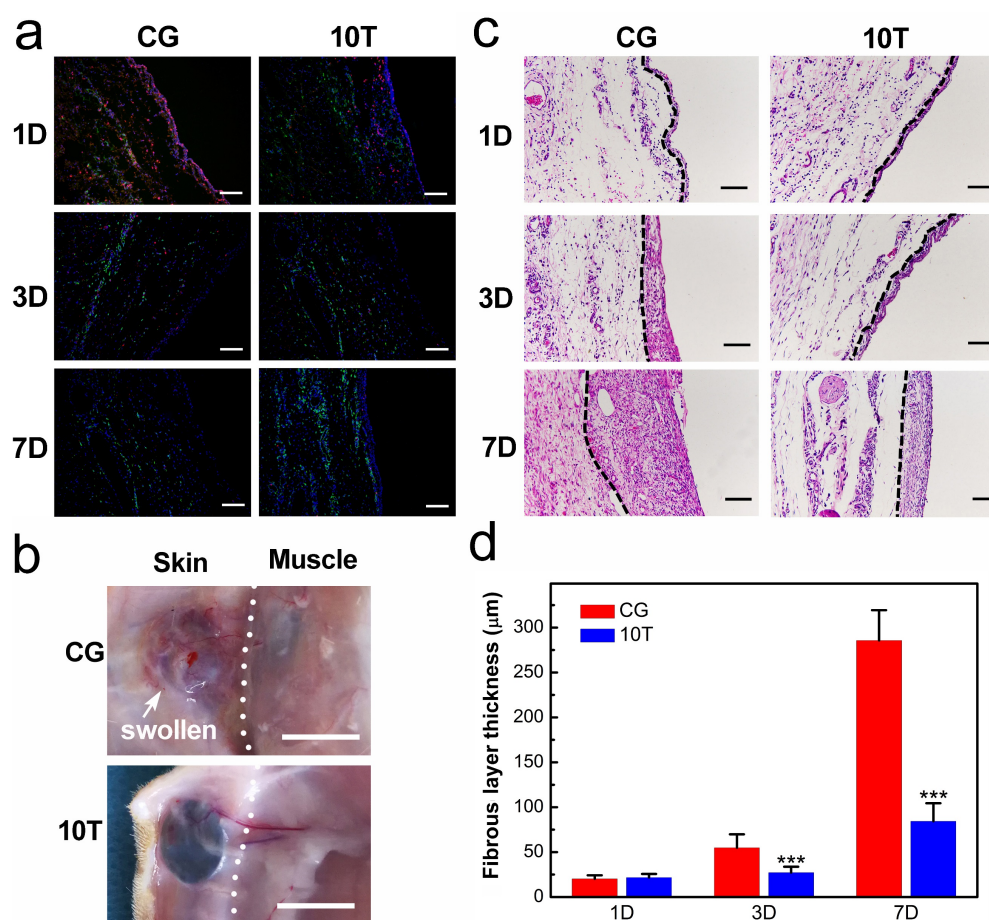

Figure 7. Inflammatory responses *in vivo*: (a) Immunofluorescent staining of the peri-implant macrophages after subcutaneous implantation of the CG and 10T samples for 1, 3 and 7 days: red (INOS, M1 marker), green (CD163, M2 marker) and blue (nuclei) with the scale bar equal to 100 μm; (b) Macroscopic view of the peri-implant tissues with the scale bar equal to 10 mm; (c) H&E staining of the peri-implant tissues after subcutaneous implantation of the CG and 10T samples for 1, 3 and 7 days with the fibrous layers are marked by dashed lines and scale bar equal to 50 μm; (d) Thickness

24

of the fibrous layers after subcutaneous implantation of the CG and 10T samples for

1, 3 and 7 days. * denotes $p < 0.05$, ** denotes $p < 0.01$ and *** denotes $p < 0.001$

compared with the CG group.

4. Discussion

4.1 Influence of HPT processing on the mechanical properties

As illustrated in Figure 2, HPT processing increases the mechanical strength and

microhardness of the Ti-45Nb alloy. The microhardness increases gradually with

increasing accumulative strain and the most pronounced hardening effect is observed

for ε of 3-3.5. HPT processing has been reported to lead to inhomogeneous grain

refinement due to the different strain at various distances from the center [37]. However,

in this study, HPT processing for 10 turns ($\varepsilon = 5.5$) produces fairly homogeneous

microhardness (Figure S3, Supporting Information) and grain refinement across the

samples. In general, after HPT processing for 10 turns, the microhardness is improved

by 18% and the ultimate tensile strength increases by 78% with fair ductility. The main

reason is the substantial grain refinement from ~77 μm to ~88 nm (Figure 1) as well as

dislocation strengthening [37], which have been observed from the Ti-45Nb alloy after

SPD processing [2,3, 6, 16].

In contrast, the elastic modulus of Ti-45Nb remains almost the same after HPT

processing (Figure 2a) in agreement with the reported results [3, 6,1 6]. Since the linear

part of the initial tensile curve corresponds to elastic deformation, Figure 2c shows that

the 10T and CG samples have the same elastic modulus because of the same slopes.

The reason stems from 100% retention of the β phase after HPT processing as

confirmed by XRD (Figure 1d). Although heat treatment can increase the strength of

25

the Ti-45Nb alloy, strengthening is offset by the drastic increase in the elastic modulus due to precipitation of the α phase [9]. Therefore, HPT processing is superior to the processing including heat treatment by producing high strength and maintaining low elastic modulus at the same time.

4.2 Influence of grain refinement on the corrosion behavior

The stability of the passive layer is crucial to corrosion protection which relies on the corrosion potential of the passive layer as well as pH, temperature and composition of the corrosion solution [19]. In the presence of halide ions (Cl^-, F^-, Br^- and I^-), the passive layer of Ti can be readily destroyed [19]. The concentrations of Cl^- in serum and interstitial body fluids are 113 and 117 mEq/L, respectively, which can severely corrode metallic implants [48]. Herein, the SBF with a chloride concentration of 143 mEq/L is employed to assess the corrosion behavior and leaching of metallic ions. According to the point defect model (PDM), local corrosion damages the passive layer of the Ti-45Nb alloy by the following steps: (1) incorporation of aggressive ions (Cl^-) from the SBF into oxygen vacancies, (2) formation of cation vacancies at the oxide/electrolyte interface, (3) diffusion of cation vacancies and subsequent annihilation by oxidation, and (4) condensation of non-annihilated vacancies to form voids leading to local detachment of the passive layer and pitting corrosion [49].

The electrochemical results disclose that the 10T sample has better corrosion resistance. As shown in Figure 3a, a quicker increase of OCP with immersion time implies faster formation of the passive film on the 10T sample and better corrosion resistance. The potentiodynamic polarization curves in Figure 3c indicate the passivation characteristics in the electrolyte and the CG, 4T and 10T samples exhibit a similar passive behavior and typical active-passive transition like pure Ti [50]. The passive region is also quite similar for all the samples. Noteworthily, the 10T sample

shows the largest corrosion potential (-0.120 V) and smallest corrosion current density (0.213 µA·cm^{-2}), whereas the CG sample shows the smallest corrosion potential (-0.228 V) and biggest corrosion current density (8.55 µA·cm^{-2}) suggesting the corrosion rate of the 10T sample is smaller.

The MS plots in Figure 3b show the impact of grain refinement on the density and diffusivity of point defects in the passive layers. The calculated value of N_d in the passive layer doped with Nb_2O_5 has been reported to be on the order of 10^{18} cm^{-3} [41] and less than 10^{20} cm^{-3} for the passive layer on pure Ti [42]. This is because Nb_2O_5 stabilizes the TiO_2 passive layer [14, 46, 47] by forming strong covalent bonds between Ti and Nb atoms [53] and creating fewer point defects in the passive layer. The N_d values determined in this study are on the order of 10^{18} cm^{-3} indicating that the Ti passive layer is incorporated with Nb_2O_5. According to Figure 3b, oxygen vacancies and/or the cation interstitials act as electron donors leading to n-type semiconducting characteristics. A larger density of oxygen vacancies and/or Ti/Nb interstitials in the passive film appears to be the main reason for the larger N_d. As shown in Figure 3b, N_d of the 10T sample is smaller than those of the 4T and CG samples, implying that grain refinement reduces the number of defects in the passive layer and increases the corrosion resistance.

According to the Nyquist plots shown in Figure 3d, the samples exhibit only one capacitance loop and the arc-like behavior. Generally, a larger diameter of the capacitive loop indicates better corrosion resistance [54]. The simulated equivalent electrical circuit [19] is generated to evaluate R_p as shown in Table 1 and the corrosion resistance follows the order of 10T > 4T > CG. The beneficial influence of surface nanostructure on corrosion resistance are also found on metallic materials produced by other methods such as sand blasting [55], ultrasonic impact treatment [56] and surface

mechanical attrition treatment [57].

4.3 Influence of grain refinement on the passive layer

The UFG structure produced by HPT processing is mostly composed of deformation-induced non-equilibrium grain boundaries which provide higher energy than those at the equilibrium state and grain interior [18]. Several phenomena of the UFG microstructure such as ultra-fast diffusion [58] and room temperature grain boundary sliding [18] have been reported. In many polycrystalline materials, grain boundaries are more prone to corrosion due to the larger energy and less perfect atomic structure [59]. Grain boundaries can also act as nucleation sites for oxide in the passive layer [60]. The influence of grain refinement on the microstructure of the passive layer depends on the corrosion mode indicated by the polarization curves, that is, active, passive, or active/passive [19]. In the active mode of corrosion, the corrosion rate is accelerated by grain refinement (e.g. magnesium [61]) but the passive mode exhibits the opposite trend [62]. Since the Ti-45Nb alloy shows the passive mode in electrochemical polarization (Figure 3c), the improved corrosion resistance can be attributed to more grain boundaries and the lower work function.

The work function, ϕ, which is the minimum energy needed to expel an electron from the surface, affects the electrochemical properties such as corrosion resistance and anodic oxidation. The energy needed to remove atoms is decided by the location of the atoms in polycrystalline materials. Atoms in defects such as grain boundaries have fewer bonds with the host lattice and can leach into the external medium more easily. The smaller work function of the 10T sample (Figure 5) confirms that this tendency also applies to Ti-45Nb. ϕ of the Ti substrate governs the band alignment at the oxide/metal contact. Figure 3b shows that the TiO_x/NbO_y passive layer is an n-type semiconductor and the Schottky barrier (Figure 8b) [45] forms a potential energy

28

barrier for electron transfer at the metal-semiconductor junction [63]. The Schottky barrier φ_B can be calculated by the Schottky-Mott rule [64]. Because the current flow across a metal-semiconductor interface depends exponentially on φ_B at an applied voltage, φ_B determines the main electrical characteristic [45]. As shown in Figure 8b, the smaller ϕ_m of the 10T sample leads to a smaller φ_B and according to the PDM theory as shown in Figure 8c, a smaller φ_B accelerates the formation of passive film to increase protection and corrosion resistance (Figure 8a). The tendency is in agreement with the results of Gu et al. who have observed that a smaller ϕ of Ti-based metallic glass gives rise to superior corrosion resistance stemming from the more protective passive film [65].

As shown in Figure 4, all the passive layers show the transition from stoichiometric TiO_2 and Nb_2O_5 to lower covalence states of Ti_2O_3, TiO, NbO_2 and NbO from the top surface to the oxide/metal interface. It is clear that grain refinement does not change the chemical composition or the n-type semiconducting nature of the passive film, but affects the thickness and defect density. Metallic Ti and Nb are present at greater depths in the 10T sample than the CG sample indicating a thicker passive oxide layer on the former. Moreover, the NbO_y layer on the 10T sample (Figure 4h) has a larger content of Nb_2O_5 (Figure 4f) and Nb^{5+} may render the TiO_2 passive layer more compact [52]. When Ti^{3+} replaces Ti^{4+}, oxygen vacancies are generated, and when Nb^{5+} exists in the passivation film, the oxygen vacancies disappear to maintain electrical neutrality [52]. The smaller number of anion vacancies mitigates migration of cation vacancies making the layer more compact [52]. Therefore, the larger concentration of Nb_2O_5 in the passive film on the 10T sample improves the anti-corrosion properties. Consistent with our reasoning, the number of defects in the passive layer of the 10T sample decreases as shown in Figure 3b.
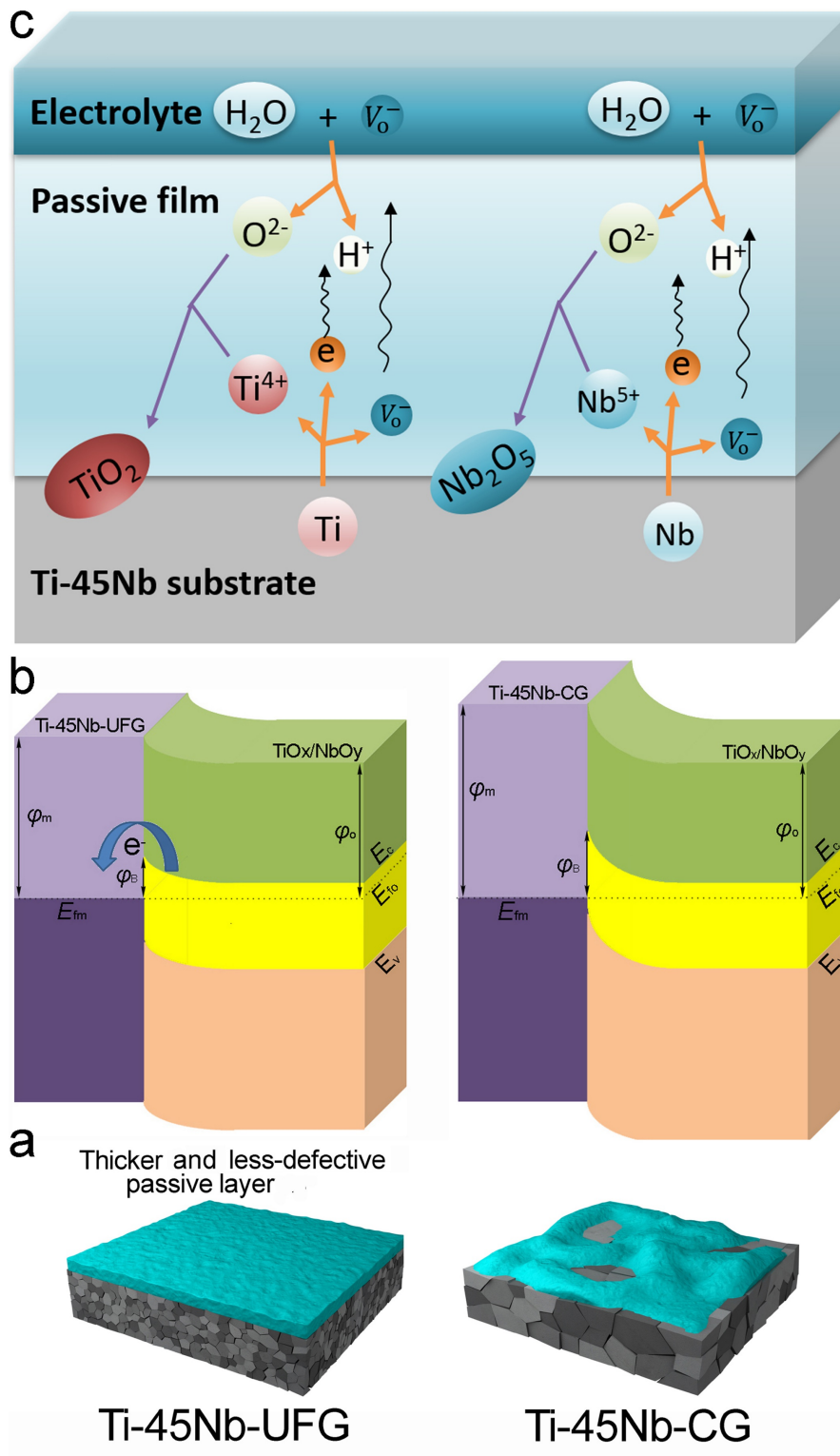
Figure 8. Schematic illustrating the influence of grain refinement on the passivation

behavior of the Ti-45Nb alloy: (a) Macroscopic illustration of the interfaces between

the passive layer and Ti-45Nb with different grain sizes [19]; (b) Schematic

illustration of the Schottky barrier at the metal-semiconductor interface with E_C, E_V, and E_{fm}/E_{fo} denoting the conduction band minimum, valence band maximum, and Fermi level, respectively, φ_m denoting the metal work function, φ_o denoting the work function and φ_B denoting the potential barrier height or Schottky barrier; (c) Schematic illustration of the evolution of the passive film on the Ti-45Nb alloy showing transport of ions and electrons.

4.4 Influence of grain refinement on the biological response

The samples undergo partial dissolution and reprecipitation in the aqueous solution and metallic ions are released gradually [48]. In this process, the amount of released ions depends on the corrosion rate and the generation time of the passive layer [48]. The OCP values in Figure 3a show that in Hank's solution at 37 ˚C, a more positive shift is observed from the 10T sample suggesting that grain refinement leads to a quicker passivation time [19]. Hence the decreased corrosion rate of the 10T sample (Figure 3b-d) combined with a quicker passivation time (Figure 3a) contribute to the reduced ion release in the solution. A similar tendency has been reported from nanostructured pure titanium [23]. Less metal ion release benefits the biocompatibility of implants [66]. For example, Ti and Nb show substantial cytotoxicity in the powder form but the bulk materials are relatively biocompatible [66] on account of less leached metallic ions. Released metallic ions are also responsible for inflammatory reactions [67] as they can spread into intercellular space to induce secretion of pro-inflammatory cytokines [68]. TNF-α is one of the cytokines released by macrophages in the inflammatory state [68,69] and TGF-β1 is one of the anti-inflammatory cytokines playing a vital role in bone formation [70]. Figure 6 shows smaller inflammatory effects on the 10T sample than the CG sample as manifested by downregulation of

31

TNF-α and upregulation of TGF-β1 in conjunction with the elongated shape of the cultured macrophages.

Our *in vivo* study confirms the anti-inflammatory effects of the 10T sample. Generally, FBRs including inflammatory cell infiltration and formation of fibrous capsules are provoked in the wound healing process after surgical implantation. Macrophages are the major infiltrating cells at the implantation sites in response to foreign materials [71,72]. As shown in Figure 7a, the sporadic macrophages in the 10T group indicate M2 polarization in line with the *in vitro* results (Figure 6 c-e). After implantation for 3 and 7 days, the tissues around the 10T sample show significantly reduced infiltrated inflammatory cells as well as much thinner fibrous layers (Figure 7c-d) indicating relieved FBRs.

5. Conclusion

HPT processing enhances the mechanical properties of the β-type Ti-45Nb alloy *via* grain boundaries strengthening. The ultimate tensile strength increases from 370 MPa to 658 MPa but the elastic modulus of the Ti-45Nb alloy remains at the low level of 61-72 GPa because the single-phase bcc β-structure is preserved during HPT processing. The Ti-45Nb sample after grain refinement has better anti-corrosion properties, because the smaller surface work function after HPT processing facilitates the formation of a thicker and less-defective surface passive layer. Furthermore, reduced corrosion rate and quick passivation mitigate leaching of pro-inflammatory metal ions and inflammatory response both *in vitro* and i*n vivo*. The strategy and materials described here provide insights into the design and fabrication of clinical orthopedic and dental implant materials with multiple functions.

Acknowledgements

References

[1]   A.R. Kilmametov, Y. Ivanisenko, A.A. Mazilkin, B.B. Straumal, A.S. Gornakova, O.B. Fabrichnaya, M.J. Kriegel, D. Rafaja, H. Hahn, The α→ω and β→ω phase transformations in Ti–Fe alloys under high-pressure torsion, Acta Mater. 144 (2018) 337–351. doi:10.1016/j.actamat.2017.10.051.

[2]   B. Völker, N. Jäger, M. Calin, M. Zehetbauer, J. Eckert, A. Hohenwarter, Influence of testing orientation on mechanical properties of Ti45Nb deformed by high pressure torsion, 114 (2017) 40–46.

[3]   M. Delshadmanesh, G. Khatibi, M.Z. Ghomsheh, M. Lederer, M. Zehetbauer, H. Danninger, Influence of microstructure on fatigue of biocompatible β-phase Ti-45Nb, Mater. Sci. Eng. A. 706 (2017) 83–94. doi:10.1016/j.msea.2017.08.098.

[4]   A. Gebert, S. Oswald, A. Helth, A. Voss, P.F. Gostin, M. Rohnke, J. Janek, M.

Calin, J. Eckert, Effect of indium (In) on corrosion and passivity of a beta-type Ti–Nb alloy in Ringer's solution, Appl. Surf. Sci. 335 (2015) 213–222. doi:10.1016/J.APSUSC.2015.02.058.

[5]   E. Eisenbarth, D. Velten, M. Müller, R. Thull, J. Breme, Biocompatibility of β-stabilizing elements of titanium alloys, Biomaterials. 25 (2004) 5705–5713. doi:10.1016/J.BIOMATERIALS.2004.01.021.

[6]   A. Panigrahi, B. Sulkowski, T. Waitz, K. Ozaltin, W. Chrominski, A. Pukenas, J. Horky, M. Lewandowska, W. Skrotzki, M. Zehetbauer, Mechanical properties, structural and texture evolution of biocompatible Ti–45Nb alloy processed by severe plastic deformation, J. Mech. Behav. Biomed. Mater. 62 (2016) 93–105.

[7]   M. Tane, T. Nakano, S. Kuramoto, M. Hara, M. Niinomi, N. Takesue, T. Yano, H. Nakajima, Low Young's modulus in Ti-Nb-Ta-Zr-O alloys: Cold working and oxygen effects, Acta Mater. 59 (2011) 6975–6988. doi:10.1016/j.actamat.2011.07.050.

[8]   H. Matsuno, Biocompatibility and osteogenesis of refractory metal implants, titanium, hafnium, niobium, tantalum and rhenium, Biomaterials. 22 (2001) 1253–1262. doi:10.1016/S0142-9612(00)00275-1.

[9]   B. Völker, V. Maier-Kiener, K. Werbach, T. Müller, S. Pilz, M. Calin, J. Eckert, A. Hohenwarter, Influence of annealing on microstructure and mechanical properties of ultrafine-grained Ti45Nb, Mater. Des. 179 (2019) 107864. doi:10.1016/j.matdes.2019.107864.

[10]   H. Liu, M. Niinomi, M. Nakai, S. Obara, H. Fujii, Improved fatigue properties with maintaining low Young's modulus achieved in biomedical beta-type

titanium alloy by oxygen addition, Mater. Sci. Eng. A. 704 (2017) 10–17. doi:10.1016/J.MSEA.2017.07.078.

[11]   M. Niinomi, M. Nakai, Titanium-Based Biomaterials for Preventing Stress Shielding between Implant Devices and Bone, Int. J. Biomater. 2011 (2011) 1–10. doi:10.1155/2011/836587.

[12]   M. Atapour, A.L. Pilchak, G.S. Frankel, J.C. Williams, Corrosion behavior of β titanium alloys for biomedical applications, Mater. Sci. Eng. C. 31 (2011) 885–891.

[13]   M. Geetha, U. Kamachi Mudali, A.. K. Gogia, R. Asokamani, B. Raj, Influence of microstructure and alloying elements on corrosion behavior of Ti–13Nb–13Zr alloy, Corros. Sci. 46 (2004) 877–892. doi:10.1016/S0010-938X(03)00186-0.

[14]   Y. Bai, Y. Deng, Y. Zheng, Y. Li, R. Zhang, Y. Lv, Q. Zhao, S. Wei, Characterization, corrosion behavior, cellular response and in vivo bone tissue compatibility of titanium–niobium alloy with low Young's modulus, Mater. Sci. Eng. C. 59 (2016) 565–576. doi:10.1016/J.MSEC.2015.10.062.

[15]   Y. Chen, N. Gao, G. Sha, S.P. Ringer, M.J. Starink, Microstructural evolution, strengthening and thermal stability of an ultrafine-grained Al–Cu–Mg alloy, Acta Mater. 109 (2016) 202–212. doi:10.1016/J.ACTAMAT.2016.02.050.

[16]   K. Ozaltin, W. Chrominski, M. Kulczyk, A. Panigrahi, J. Horky, M. Zehetbauer, M. Lewandowska, Enhancement of mechanical properties of biocompatible Ti-45Nb alloy by hydrostatic extrusion, J. Mater. Sci. 49 (2014) 6930–6936. doi:10.1007/s10853-014-8397-7.

[17]   J.L. Gilbert, Corrosion in the human body: Metallic implants in the complex

body environment, Corrosion. 73 (2017) 1478–1495. doi:10.5006/2563.

[18] H. Miyamoto, Corrosion of ultrafine grained materials by severe plastic deformation, an overview, Mater. Trans. 57 (2016) 559–572. doi:10.2320/matertrans.M2015452.

[19] H. Garbacz, A. Królikowski, Corrosion resistance of nanocrystalline titanium, in: Nanocrystalline Titan., Elsevier, 2018: pp. 145–173. doi:10.1016/B978-0-12-814599-9.00008-0.

[20] Y.J. Bai, Y.B. Wang, Y. Cheng, F. Deng, Y.F. Zheng, S.C. Wei, Comparative study on the corrosion behavior of Ti-Nb and TMA alloys for dental application in various artificial solutions, Mater. Sci. Eng. C. 31 (2011) 702–711. doi:10.1016/j.msec.2010.12.010.

[21] Y. Li, J. Xu, Is niobium more corrosion-resistant than commercially pure titanium in fluoride-containing artificial saliva?, Electrochim. Acta. 233 (2017) 151–166. doi:10.1016/j.electacta.2017.03.015.

[22] D.D. MacDonald, The history of the Point Defect Model for the passive state: A brief review of film growth aspects, in: Electrochim. Acta, Pergamon, 2011: pp. 1761–1772. doi:10.1016/j.electacta.2010.11.005.

[23] J. Lu, Y.Y. Zhang, W. Huo, W. Zhang, Y. Zhao, Y.Y. Zhang, Electrochemical corrosion characteristics and biocompatibility of nanostructured titanium for implants, Appl. Surf. Sci. 434 (2018) 63–72.

[24] A. Sotniczuk, D. Kuczyńska-Zemła, P. Kwaśniak, M. Thomas, H. Garbacz, Corrosion behavior of Ti-29Nb-13Ta-4.6Zr and commercially pure Ti under simulated inflammatory conditions – comparative effect of grain refinement and

non-toxic β phase stabilizers, Electrochim. Acta. 312 (2019) 369–379. doi:10.1016/j.electacta.2019.04.138.

[25]   J. Li, S.J. Li, Y.L. Hao, H.H. Huang, Y. Bai, Y.Q. Hao, Z. Guo, J.Q. Xue, R. Yang, Electrochemical and surface analyses of nanostructured Ti-24Nb-4Zr-8Sn alloys in simulated body solution, Acta Biomater. 10 (2014) 2866–2875. doi:10.1016/j.actbio.2014.02.032.

[26]   D.C. Hansen, Metal Corrosion in the Human Body: The Ultimate Bio-Corrosion Scenario, Interface. (2008). doi:10.3390/ma5010135.

[27]   J.C. Wang, W.D. Yu, H.S. Sandhu, F. Betts, S. Bhuta, R.B. Delamarter, Metal Debris From Titanium Spinal Implants, Spine (Phila. Pa. 1976). 24 (1999) 899–903. doi:10.1097/00007632-199905010-00011.

[28]   S.B. Goodman, Wear particles, periprosthetic osteolysis and the immune system, Biomaterials. 28 (2007) 5044–5048. doi:10.1016/j.biomaterials.2007.06.035.

[29]   S. Franz, S. Rammelt, D. Scharnweber, J.C. Simon, Immune responses to implants - A review of the implications for the design of immunomodulatory biomaterials, Biomaterials. 32 (2011) 6692–6709. doi:10.1016/j.biomaterials.2011.05.078.

[30]   K. Ma, H. Wen, T. Hu, T.D. Topping, D. Isheim, D.N. Seidman, E.J. Lavernia, J.M. Schoenung, Mechanical behavior and strengthening mechanisms in ultrafine grain precipitation-strengthened aluminum alloy, Acta Mater. 62 (2014) 141–155. doi:10.1016/J.ACTAMAT.2013.09.042.

[31]   W.C. Oliver, G.M. Pharr, Measurement of hardness and elastic modulus by instrumented indentation: Advances in understanding and refinements to

methodology, J. Mater. Res. 19 (2004) 3–20. doi:10.1557/jmr.2004.19.1.3.

[32] G.T. Burstein, A hundred years of Tafel's Equation: 1905-2005, Corros. Sci. 47 (2005) 2858–2870. doi:10.1016/j.corsci.2005.07.002.

[33] Y.T. Zhu, J.Y. Huang, J. Gubicza, T. Ungár, Y.M. Wang, E. Ma, R.Z. Valiev, Nanostructures in Ti processed by severe plastic deformation, J. Mater. Res. 18 (2003) 1908–1917. doi:DOI: 10.1557/JMR.2003.0267.

[34] A.A. Popov, I.Y. Pyshmintsev, S.L. Demakov, A.G. Illarionov, T.C. Lowe, A. V Sergeyeva, R.Z. Valiev, Structural and mechanical properties of nanocrystalleve titanium processed by severe plastic deformation, Scr. Mater. 37 (1997) 1089–1094. doi:http://dx.doi.org/10.1016/S1359-6462(97)00210-8.

[35] A. Sergueeva, V. Stolyarov, R. Valiev, A. Mukherjee, Advanced mechanical properties of pure titanium with ultrafine grained structure, Scr. Mater. 45 (2001) 747–752. doi:http://dx.doi.org/10.1016/S1359-6462(01)01089-2.

[36] A. Panigrahi, B. Sulkowski, T. Waitz, K. Ozaltin, W. Chrominski, A. Pukenas, J. Horky, M. Lewandowska, W. Skrotzki, M. Zehetbauer, Mechanical properties, structural and texture evolution of biocompatible Ti–45Nb alloy processed by severe plastic deformation, J. Mech. Behav. Biomed. Mater. 62 (2016) 93–105. doi:10.1016/j.jmbbm.2016.04.042.

[37] A.P. Zhilyaev, T.G. Langdon, Using high-pressure torsion for metal processing: Fundamentals and applications, Prog. Mater. Sci. 53 (2008) 893–979. doi:http://dx.doi.org/10.1016/j.pmatsci.2008.03.002.

[38] ASTM F67 - 13 Standard Specification for Unalloyed Titanium, for Surgical Implant Applications (UNS R50250, UNS R50400, UNS R50550, UNS

R50700), (n.d.).
https://www.astm.org/DATABASE.CART/HISTORICAL/F67-13.htm
(accessed December 28, 2020).

[39] I. Milošev, G. Žerjav, J.M. Calderon Moreno, M. Popa, Electrochemical properties, chemical composition and thickness of passive film formed on novel Ti-20Nb-10Zr-5Ta alloy, Electrochim. Acta. 99 (2013) 176–189. doi:10.1016/j.electacta.2013.03.086.

[40] B. Munirathinam, R. Narayanan, L. Neelakantan, Electrochemical and semiconducting properties of thin passive film formed on titanium in chloride medium at various pH conditions, Thin Solid Films. 598 (2016) 260–270. doi:10.1016/j.tsf.2015.12.025.

[41] M.T. Woldemedhin, D. Raabe, A.W. Hassel, Characterization of thin anodic oxides of Ti-Nb alloys by electrochemical impedance spectroscopy, in: Electrochim. Acta, Pergamon, 2012: pp. 324–332. doi:10.1016/j.electacta.2012.06.029.

[42] A. Fattah-alhosseini, A.R. Ansari, Y. Mazaheri, M.K. Keshavarz, Effect of immersion time on the passive and electrochemical response of annealed and nano-grained commercial pure titanium in Ringer's physiological solution at 37 °C, Mater. Sci. Eng. C. 71 (2017) 771–779. doi:10.1016/j.msec.2016.10.057.

[43] M.C.K. Sellers, E.G. Seebauer, Measurement method for carrier concentration in TiO2 via the Mott-Schottky approach, Thin Solid Films. 519 (2011) 2103–2110. doi:10.1016/j.tsf.2010.10.071.

[44] Y.L. Guo, L.N. Jia, H.R. Zhang, B. Kong, Y.L. Huang, H. Zhang, Microstructure

and High-Temperature Oxidation Behavior of Dy-Doped Nb–Si-Based Alloys, Acta Metall. Sin. (English Lett. 31 (2018) 742–752. doi:10.1007/s40195-018-0701-0.

[45] W. Mönch, Metal-semiconductor contacts: electronic properties, Surf. Sci. 299–300 (1994) 928–944. doi:10.1016/0039-6028(94)90707-2.

[46] S.M. Hamlet, S. Ivanovski, Inflammatory cytokine response to titanium surface chemistry and topography, in: Immune Response to Implant. Mater. Devices Impact Immune Syst. Success an Implant, Springer International Publishing, 2016: pp. 151–167. doi:10.1007/978-3-319-45433-7_8.

[47] W.-C. Xu, X. Dong, J.-L. Ding, J.-C. Liu, J.-J. Xu, Y.-H. Tang, Y.-P. Yi, C. Lu, W. Yang, J.-S. Yang, Y. Gong, J.-L. Zhou, Nanotubular TiO_2 regulates macrophage M2 polarization and increases macrophage secretion of VEGF to accelerate endothelialization via the ERK1/2 and PI3K/AKT pathways, Int. J. Nanomedicine. Volume 14 (2019) 441–455. doi:10.2147/IJN.S188439.

[48] T. Hanawa, Metal ion release from metal implants, in: Mater. Sci. Eng. C, Elsevier, 2004: pp. 745–752. doi:10.1016/j.msec.2004.08.018.

[49] Z. Jiang, X. Dai, T. Norby, H. Middleton, Investigation of pitting resistance of titanium based on a modified point defect model, Corros. Sci. 53 (2011) 815–821. doi:10.1016/j.corsci.2010.11.015.

[50] L. Wang, H. Yu, K. Wang, H. Xu, S. Wang, D. Sun, Local Fine Structural Insight into Mechanism of Electrochemical Passivation of Titanium, ACS Appl. Mater. Interfaces. 8 (2016) 18608–18619. doi:10.1021/acsami.6b05080.

[51] Y. Chen, P. Han, A. Dehghan-Manshadi, D. Kent, S. Ehtemam-Haghighi, C.

Jowers, M. Bermingham, T. Li, J. Cooper-White, M.S. Dargusch, Sintering and biocompatibility of blended elemental Ti-xNb alloys, J. Mech. Behav. Biomed. Mater. 104 (2020) 103691. doi:10.1016/j.jmbbm.2020.103691.

[52] P.F. Ji, B. Li, B.H. Chen, F. Wang, W. Ma, X.Y. Zhang, M.Z. Ma, R.P. Liu, Effect of Nb addition on the stability and biological corrosion resistance of Ti-Zr alloy passivation films, Corros. Sci. 170 (2020) 108696. doi:10.1016/j.corsci.2020.108696.

[53] S.Y. Yu, J.R. Scully, C.M. Vitus, Influence of Niobium and Zirconium Alloying Additions on the Anodic Dissolution Behavior of Activated Titanium in HCl Solutions, J. Electrochem. Soc. 148 (2001) B68. doi:10.1149/1.1337605.

[54] W.T. Huo, L.Z. Zhao, W. Zhang, J.W. Lu, Y.Q. Zhao, Y.S. Zhang, In vitro corrosion behavior and biocompatibility of nanostructured Ti6Al4V, Mater. Sci. Eng. C. 92 (2018) 268–279. doi:10.1016/j.msec.2018.06.061.

[55] X.Y. Wang, D.Y. Li, Mechanical and electrochemical behavior of nanocrystalline surface of 304 stainless steel, Electrochim. Acta. 47 (2002) 3939–3947. doi:10.1016/S0013-4686(02)00365-1.

[56] Y.N. Petrov, G.I. Prokopenko, B.N. Mordyuk, M.A. Vasylyev, S.M. Voloshko, V.S. Skorodzievski, V.S. Filatova, Influence of microstructural modifications induced by ultrasonic impact treatment on hardening and corrosion behavior of wrought Co-Cr-Mo biomedical alloy, Mater. Sci. Eng. C. 58 (2016) 1024–1035. doi:10.1016/j.msec.2015.09.004.

[57] D. V. Tchana Nkonta, F. Simescu-Lazar, R. Drevet, O. Aaboubi, J. Fauré, D. Retraint, H. Benhayoune, Influence of the surface mechanical attrition treatment

(SMAT) on the corrosion behavior of Co28Cr6Mo alloy in Ringer's solution, J. Solid State Electrochem. 22 (2018) 1091–1098. doi:10.1007/s10008-017-3851-5.

[58] S. V. Divinski, G. Reglitz, I.S. Golovin, M. Peterlechner, R. Lapovok, Y. Estrin, G. Wilde, Effect of heat treatment on diffusion, internal friction, microstructure and mechanical properties of ultra-fine-grained nickel severely deformed by equal-channel angular pressing, Acta Mater. 82 (2015) 11–21. doi:10.1016/j.actamat.2014.08.064.

[59] R.W. Revie, Uhlig's Corrosion Handbook: Third Edition, John Wiley and Sons, Hoboken, NJ, USA, 2011. doi:10.1002/9780470872864.

[60] K.D. Ralston, N. Birbilis, C.H.J. Davies, Revealing the relationship between grain size and corrosion rate of metals, Scr. Mater. 63 (2010) 1201–1204. doi:10.1016/j.scriptamat.2010.08.035.

[61] D. Song, A. Bin Ma, J. Jiang, P. Lin, D. Yang, J. Fan, Corrosion behavior of equal-channel-angular-pressed pure magnesium in NaCl aqueous solution, Corros. Sci. 52 (2010) 481–490. doi:10.1016/j.corsci.2009.10.004.

[62] K.D. Ralston, N. Birbilis, Effect of Grain Size on Corrosion: A Review, Corrosion. 66 (2010) 75005–75013. doi:10.5006/1.3462912.

[63] C.M. Aldao, Surface and interface electronic properties of tin oxide, in: Tin Oxide Mater., Elsevier, 2020: pp. 101–132. doi:10.1016/b978-0-12-815924-8.00005-0.

[64] R.T. Tung, The physics and chemistry of the Schottky barrier height, Appl. Phys. Rev. 1 (2014) 011304. doi:10.1063/1.4858400.

[65] J.L. Gu, Y. Shao, H.T. Bu, J.L. Jia, K.F. Yao, An abnormal correlation between electron work function and corrosion resistance in Ti-Zr-Be-(Ni/Fe) metallic glasses, Corros. Sci. 165 (2020) 108392. doi:10.1016/j.corsci.2019.108392.

[66] Y. Li, C. Wong, J. Xiong, P. Hodgson, C. Wen, Cytotoxicity of titanium and titanium alloying elements., J. Dent. Res. 89 (2010) 493–7. doi:10.1177/0022034510363675.

[67] S. Spriano, S. Yamaguchi, F. Baino, S. Ferraris, A critical review of multifunctional titanium surfaces: New frontiers for improving osseointegration and host response, avoiding bacteria contamination, Acta Biomater. 79 (2018) 1–22. doi:10.1016/j.actbio.2018.08.013.

[68] I. Catelas, A. Petit, D.J. Zukor, J. Antoniou, O.L. Huk, TNF-α secretion and macrophage mortality induced by cobalt and chromium ions in vitro - Qualitative analysis of apoptosis, Biomaterials. 24 (2003) 383–391. doi:10.1016/S0142-9612(02)00351-4.

[69] J. Lu, T.J. Webster, Reduced immune cell responses on nano and submicron rough titanium, Acta Biomater. 16 (2015) 223–231. doi:10.1016/j.actbio.2015.01.036.

[70] S. Kasagi, W. Chen, TGF-beta1 on osteoimmunology and the bone component cells, Cell Biosci. 3 (2013) 4. doi:10.1186/2045-3701-3-4.

[71] N. Donos, S. Hamlet, N.P. Lang, G.E. Salvi, G. Huynh-Ba, D.D. Bosshardt, S. Ivanovski, Gene expression profile of osseointegration of a hydrophilic compared with a hydrophobic microrough implant surface, Clin. Oral Implants Res. 22 (2011) 365–372. doi:10.1111/j.1600-0501.2010.02113.x.

[72] H.-J. Han, S. Kim, D.-H. Han, Multifactorial Evaluation of Implant Failure: A 19-year Retrospective Study, Int. J. Oral Maxillofac. Implants. 29 (2014) 303–310. doi:10.11607/jomi.2869.